LETTERS
https://doi.org/10.1038/s41567-019-0652-z

nature physics

Quantum state tomography across the exceptional point in a single dissipative qubit

M. Naghiloo[1], M. Abbasi[1], Yogesh N. Joglekar[2*] and K. W. Murch[1,3*]

Open physical systems can be described by effective non-Hermitian Hamiltonians that characterize the gain or loss of energy or particle numbers from the system. Experimental realization of optical[1–7] and mechanical[8–13] non-Hermitian systems has been reported, demonstrating functionalities such as lasing[14–16], topological features[7,17–19], optimal energy transfer[20,21] and enhanced sensing[22,23]. Such realizations have been limited to classical (wave) systems in which only the amplitude information, not the phase, is measured. Thus, the effects of a systems's proximity to an exceptional point—a degeneracy of such non-Hermitian Hamiltonians where the eigenvalues and corresponding eigenmodes coalesce[24–29]—on its quantum evolution remain unexplored. Here, we use post-selection on a three-level superconducting transmon circuit to carry out quantum state tomography of a single dissipative qubit in the vicinity of its exceptional point. We observe the spacetime reflection symmetry-breaking transition[30,31] at zero detuning, decoherence enhancement at finite detuning and a quantum signature of the exceptional point in the qubit relaxation state. Our experiments show phenomena associated with non-Hermitian physics such as non-orthogonality of eigenstates in a fully quantum regime, which could provide a route to the exploration and harnessing of exceptional point degeneracies for quantum information processing.

In introductory treatments of quantum mechanics, one typically assumes that a Hamiltonian describing a physical system is Hermitian, thus ensuring the reality of energy eigenvalues and a unitary time evolution. In recent years there has been growing interest in non-Hermitian systems, particularly those with space-time reflection (parity–time; $\mathcal{PT}$) symmetry that exhibit transitions from purely real to complex conjugate spectra. A canonical example of a $\mathcal{PT}$-symmetric system is shown in Fig. 1a and consists of a bipartite system with balanced gain (part A) and loss (part B). Such systems have been experimentally studied in the classical domain. The central feature of these systems is a transition from broken to unbroken $\mathcal{PT}$ symmetry. When the coupling, given by rate J, between the two parts is larger than the gain–loss rate $\gamma_{\pm}$, the system exhibits a real spectrum and simultaneous eigenmodes of both the Hamiltonian and the antilinear $\mathcal{PT}$ operator; yet when the coupling is small, this $\mathcal{PT}$ symmetry is broken by the emergence of complex conjugate eigenvalues. These two phases are joined by an exceptional point (EP). The EP degeneracy also occurs for a bipartite system with imbalanced losses. The schematic in Fig. 1b displays such a system in which parts A and B are coupled and part B exhibits loss. Here, we extend these studies to a fully quantum limit where these parts are realized as quantum energy levels—with no classical counterparts—in which the loss corresponds to transitions outside that manifold of states. This two-level system in the presence of coupling produced by a drive with detuning Δ can be described by an effective non-Hermitian Hamiltonian ($\hbar = 1$):

$$H_{\rm eff} = J\left(|f\rangle\langle e| + |e\rangle\langle f|\right) + (\Delta - i\gamma_e/2)|e\rangle\langle e| \qquad (1)$$

where $|e\rangle$ and $|f\rangle$ denote the first and second excited states of the quantum system and γ_e is the occupation-number loss rate to the ground state $|g\rangle$ (Fig. 1b). At zero detuning, the complex eigenvalues of $H_{\rm eff}$ have different imaginary components at $J < \gamma_e/4$, and the system is in the $\mathcal{PT}$-broken phase. At stronger coupling, past the EP at $J = \gamma_e/4$, the imaginary components for the two dissipative eigenmodes coincide, and the system is in the $\mathcal{PT}$-symmetric phase. When $\Delta \neq 0$, the two complex eigenvalues $\lambda_{\pm}$ of $H_{\rm eff}$ (equation (1)) have different real and imaginary parts. Here, the qubit dynamics is governed by eigenmode energy differences $\mathrm{Re}(\delta\lambda(\Delta, J))$ (Fig. 1c) and $\mathrm{Im}(\delta\lambda(\Delta, J))$ (Fig. 1d), where Re and Im indicate real and imaginary parts, respectively, and the eigenvalue difference $\delta\lambda$ is given by $\delta\lambda = (\lambda_+ - \lambda_-) = \sqrt{4J^2 - (\Delta - i\gamma_e/2)^2}$

Our experiment comprises a transmon circuit formed by a pair of Josephson junctions in a superconducting quantum interference device (SQUID) geometry shunted by a capacitor (Fig. 1e). The transmon circuit exhibits several quantum energy levels that can be individually addressed with narrow-bandwidth microwave pulses. By applying a magnetic flux through the SQUID loop, we can tune the spacing between energy levels. The coupling Hamiltonian $J\sigma_x = J\left(|f\rangle\langle e| + |e\rangle\langle f|\right)$ is realized by a coherent resonant drive of variable amplitude and detuning.

The transmon circuit is embedded in a three-dimensional waveguide cavity. The dispersive interaction between the transmon circuit and fundamental electromagnetic mode of the cavity results in a state-dependent shift in the cavity frequency. This frequency shift is detected by probing the cavity with a weak microwave tone; the resulting state-dependent phase shift is detected with homodyne measurement using a Josephson parametric amplifier. The lowest energy level $|g\rangle$ is the stable ground state, and we use it as an effective continuum—an environment that is 'outside' of the submanifold of states $|e\rangle$ and $|f\rangle$ that form the qubit system under investigation. To implement $H_{\rm eff}$, we require the respective energy decay rates $\gamma_e \gg \gamma_f$. The presence of a finite decay rate γ_f shifts the EP to $J = \gamma/4 = (\gamma_e - \gamma_f)/4$. We achieve this hierarchy of decay rates by inserting an impedance mismatching element between the cavity and parametric amplifier. This causes an interference in the cavity field that alternately suppresses and enhances the density of states in the transmission line, resulting in a frequency dependence of the Purcell decay rate. Thus, by tuning the transition frequency between the $|g\rangle$ and $|e\rangle$ states to regions where the density of states is enhanced, we enhance the decay rate of the $|e\rangle$ state.

[1]Department of Physics, Washington University, St. Louis, MO, USA. [2]Department of Physics, Indiana University–Purdue University Indianapolis, Indianapolis, IN, USA. [3]Institute for Materials Science and Engineering, St. Louis, MO, USA. *e-mail: yojoglek@iupui.edu; murch@physics.wustl.edu

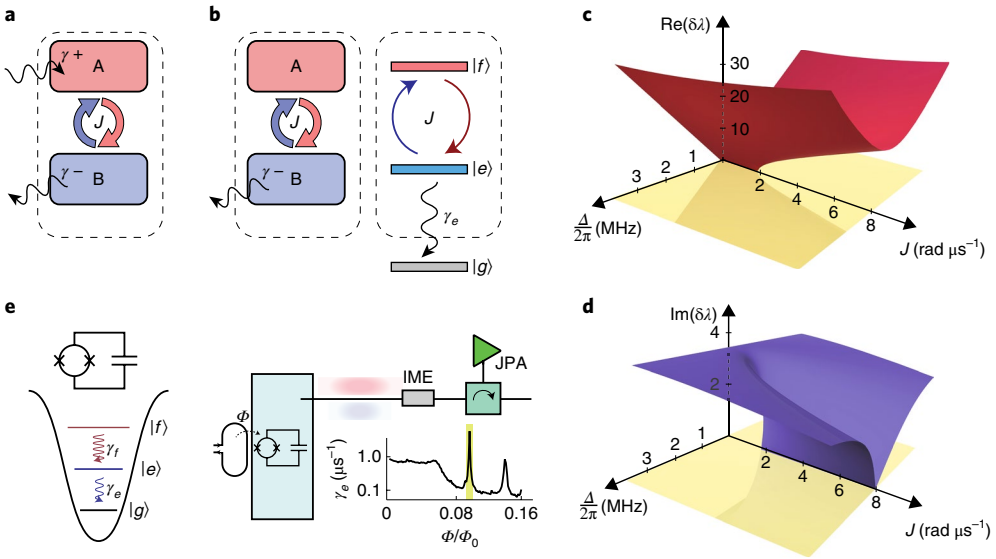

Fig. 1 | Experimental overview. a, A system with balanced gain and loss exhibits $\mathcal{PT}$ symmetry. **b**, Systems with mode-selective losses where one mode exhibits loss manifest the same topological features as $\mathcal{PT}$-symmetric systems with balanced gain and loss. We realize these features in the quantum regime by using a sub-manifold of quantum states; transitions out of this sub-manifold are described by H_{eff}. **c**,**d**, The real (**c**) and imaginary (**d**) parts of $\delta\lambda$ show an EP at $J=\gamma_e/4$ along the J axis (zero detuning). The yellow shading depicts the region explored in this experiment, with $\Delta=\omega_d-\omega_q$, where ω_d is the drive frequency and ω_q is the transition frequency between the $|e\rangle$ and $|f\rangle$ levels. **e**, The experiment uses the three lowest levels of a transmon circuit. The circuit is embedded in a three-dimensional cavity, and an impedance mismatch element (IME) is used to shape the density of states that drive the decay of the transmon states through spontaneous emission. A Josephson parametric amplifier (JPA) is used for high-fidelity readout of the transmon state. As shown in the inset, different decay rates can be obtained by threading a d.c. magnetic flux Φ, with Φ_0 the magnetic flux quantum, through the SQUID loop, which tunes the frequency of the transmon energy levels. The highlighted region indicates the bias condition used for the experiment.

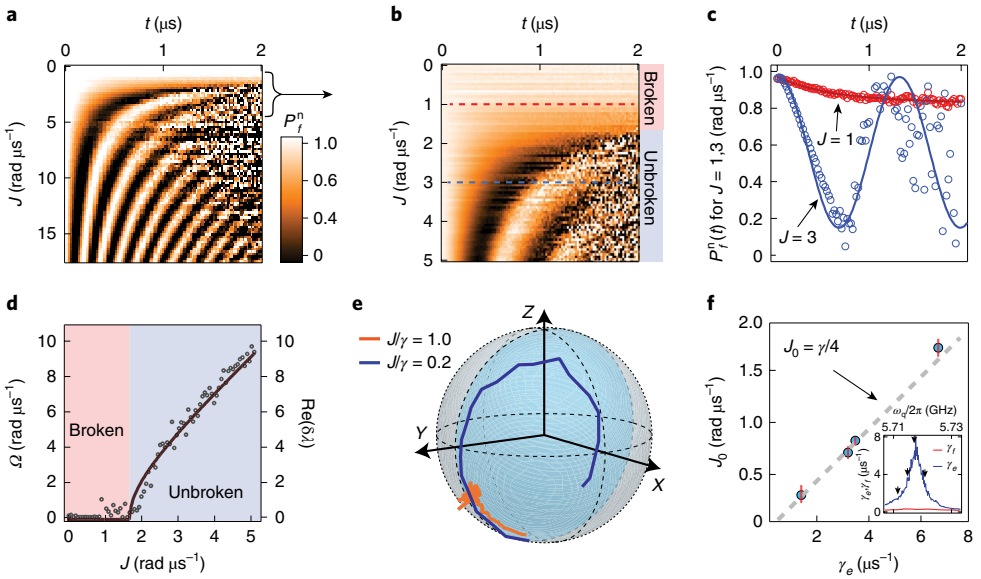

Fig. 2 | $\mathcal{PT}$ symmetry-breaking transition in a single dissipative qubit. a, Colour map of P_f^n versus t for various values of J. **b**, Detail of P_f^n for small values of J, highlighting the transition from the $\mathcal{PT}$-broken to the $\mathcal{PT}$-unbroken phase. **c**, The P_f^n versus time plot for two values of J ($J=1$, red circles; $J=3$, blue circles) from **b** show oscillatory to steady-state behaviour. The solid lines are curve fits. **d**, The extracted Ω for different values of J. The solid line indicates a fit to the analytical result $\Omega=\text{Re}(\delta\lambda)$. **e**, Evolution of the quantum state in the Bloch sphere for parameters in the $\mathcal{PT}$-broken region (orange) for $t=[0, 2]$ μs, and in the $\mathcal{PT}$-symmetric region (blue) for $t=[0, 0.4]$ μs. Both time intervals correspond to the same scaled time $2Jt$. **f**, By tuning the transition frequencies of the transmon, different decay rates γ_e can be obtained (inset). The $\mathcal{PT}$ symmetry-breaking threshold is obtained as in **d** for four different values of the decay rate (blue circles), showing good agreement with $J_0=\gamma/4$. The error bars indicate the estimated error of the fit.

We first investigate the $\mathcal{PT}$ symmetry-breaking transition, which occurs when $\Delta=0$. We tune the transmon such that $\gamma_e=6.7\,\mu s^{-1}$ and $\gamma_f=0.25\,\mu s^{-1}$. We then initialize the system in the state $|f\rangle$ with $J=0$, and at time $t=0$, we switch J to a finite value for a variable period of time. The experimental sequence is concluded with a projective measurement of the transmon energy. Evolution under

$H_{\rm eff}$ leads to exponential decay of the norm of a given initial state. Experimentally, we focus on the evolution in the $\{|e\rangle, |f\rangle\}$ qubit manifold, which results in normalized populations $P_f^{\rm n} = P_f/(P_f + P_e)$ and $P_e^{\rm n} = P_e/(P_f + P_e) = 1 - P_f^{\rm n}$. This is achieved through post-selection; experimental sequences conclude with a projective measurement of the transmon in the energy basis, and only experiments in which the transmon remains in the qubit manifold are included in the analysis. Thus, for longer experimental durations, the success rate decreases exponentially.

We now characterize the $\mathcal{PT}$ symmetry-breaking transition using the observed experimental signatures in the populations and the coherences in the $\{|e\rangle, |f\rangle\}$ qubit manifold. In Fig. 2a we show $P_f^{\rm n}$ versus time for different coupling rates J. For a large J we observe oscillatory dynamics in $P_f^{\rm n}$. These Rabi oscillations occur because the initial state $|f\rangle$ can be expressed as a superposition of eigenmodes of $H_{\rm eff}$ with corresponding time evolution $e^{-i\lambda_\pm t}$; the equal imaginary parts of $\lambda_\pm$ for $J > \gamma/4$ result in the oscillatory evolution at angular frequency Ω for the post-selected occupation probabilities. This region is referred to as the $\mathcal{PT}$-unbroken region. The time evolution of $P_f^{\rm n}$ shows a striking transition at the finite coupling rate, as detailed in Fig. 2b. Here, we observe that when $J < \gamma/4$, the oscillations cease due to the vanishing real parts of $\lambda_\pm$. This is referred to as the $\mathcal{PT}$-broken region. Figure 2c displays time-trace cuts from Fig. 2b in the broken and unbroken regions with decaying and oscillatory behaviour, respectively. Although Fig. 2 displays only data for which the transmon did not leave the $\{|e\rangle, |f\rangle\}$ qubit manifold, the post-selection on the qubit manifold leads to measurement back-action favouring the $|f\rangle$ state, leaving a clear signature of the decay in the temporal evolution within this manifold.

The $\mathcal{PT}$ symmetry-breaking transition can be quantified by looking at the Rabi frequency Ω as a function of the coupling rate. This Ω is obtained from a simple, exponentially damped sinusoidal fit to $P_f^{\rm n}(t)$ (Fig. 2c). In Fig. 2d we plot the observed Ω versus J, which displays a square-root singularity that is associated with increased sensitivity near the EP[22,23]. The solid curve displays a fit to $\mathrm{Re}\delta\lambda = 2\mathrm{Re}\sqrt{J^2 - J_0^2}$, where J_0 is the sole free parameter. From the fit we find $J_0 = 1.71 \pm 0.07\,\mu\mathrm{s}^{-1}$, which is in agreement with the expected value based on the independently measured decay rates $(\gamma_e - \gamma_f)/4 = \gamma/4 = 1.61\,\mu\mathrm{s}^{-1}$.

Next, we characterize the evolution of the qubit in the broken and unbroken regimes using quantum state tomography. Figure 2e displays $y \equiv \langle\sigma_y\rangle$ and $z \equiv \langle\sigma_z\rangle$ (the initial state and Hamiltonian confine the evolution to the Y–Z plane of the Bloch sphere) versus time for two different experimental conditions. While evolution in the $\mathcal{PT}$-symmetric phase shows oscillatory behaviour, in the $\mathcal{PT}$-broken phase the state approaches a fixed point in the Y–Z plane. Both state trajectories are plotted for the same scaled time interval, $0 \le 2Jt \le 5.24$ rad, highlighting the difference in quantum evolution in the symmetric and broken phases.

We repeat the experiment for different values of γ by tuning the flux threading the transmon SQUID loop and thereby changing the SQUID inductance, placing the transmon levels in contact with different parts of the engineered bath, as depicted by arrows in Fig. 2f (inset). Figure 2f shows the results from four different experiments. The $\mathcal{PT}$ transition determined from fits of Ω for different values of J (as in Fig. 2d) is in close agreement with the analytical result $J_0 = \gamma/4$.

In Fig. 3 we study the locations of the eigenstates of $H_{\rm eff}$ on the Bloch sphere as the system traverses the $\mathcal{PT}$ transition at the second-order EP. We prepare different states of the qubit given by polar (θ) and azimuthal (ϕ) angles on the Bloch sphere. In the broken region (Fig. 3a) the eigenstates appear as places where $\delta P_f^{\rm n} = P_f^{\rm n}(t=0) - P_f^{\rm n}(t = 500\,\mathrm{ns})$ is zero for different initial preparations in the Y–Z plane. For the unbroken region (Fig. 3b), these stationary states appear on the X–Y plane. The expected stationary states, which are based on the diagonalization of $H_{\rm eff}$, are represented by dashed lines. The non-orthogonality of the eigenstates across the $\mathcal{PT}$ transition, including in the vicinity of the EP, is characterized in terms of the overlap $|\langle+|-\rangle|$ of the two eigenstates, displayed in Fig. 3c. The dashed line indicates the theoretical value $|\langle+|-\rangle| = \min(x, 1/x)$, where $x = 4J/\gamma$.

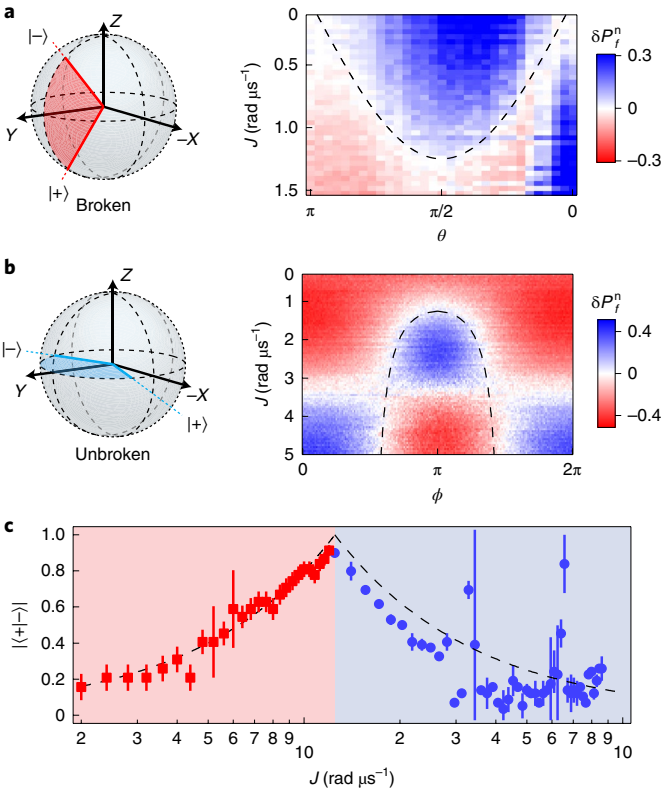

Fig. 3 | Non-orthogonality of eigenstates in the vicinity of the EP. **a**,**b**, The eigenstates in the broken (unbroken) region lie in the Y–Z (X–Y) plane (Bloch spheres). The fractional change in $P_f^{\rm n}$ for different polar (**a**) and azimuthal (**b**) preparation angles (right panels). The calculated angles for the eigenstates in the broken (**a**) and unbroken (**b**) regions are indicated as dashed lines. **c**, The overlap between the two eigenstates in both regions satisfies $|\langle+|-\rangle| = \min(x, 1/x)$ (dashed line) where $x = 4J/\gamma$. The overlap was determined from the preparation angles for the eigenstates, which were found from the zero-crossing of the $\delta P_f^{\rm n}$ plots, determined from $\min(\mathrm{abs}(\delta P_f^{\rm n}))$. The error in the preparation angle was estimated as the distance to the next-nearest minima, and the error bars in **c** indicate this error propagated to the inner product. For some data points, the error bar is smaller than the marker.

With access to the quantum coherent dynamics in the vicinity of the EP, it is natural to investigate the role of decoherence in this regime. As shown in Fig. 1c,d, the eigenvalue difference $\delta\lambda$ of $H_{\rm eff}$ exhibits rich dependence on J and Δ, which in turn determine the time evolution of the dissipative qubit. Figure 4a depicts the time evolution of the qubit state given by Bloch coordinates $x(t)$, $y(t)$ and $z(t)$, which were measured with quantum state tomography for different values of the detuning. In the $\mathcal{PT}$-symmetric phase, we fit the oscillations to determine both Ω and the Rabi oscillation damping rate $\Gamma_{\rm R}$ for different detunings, yielding, respectively, the real and imaginary parts of $\delta\lambda$ (Fig. 4b). At $\Delta = 0$, the eigenmode decay rates are equal, and we observe only a residual, small coherence damping in the qubit manifold, characterized by $\Gamma_0 = 0.6\,\mu\mathrm{s}^{-1}$; this damping is larger than expected from the small γ_f and is primarily due to charge and flux noise. As $|\Delta|$ increases, the difference in the eigenmode decay rates leads to faster coherence damping.

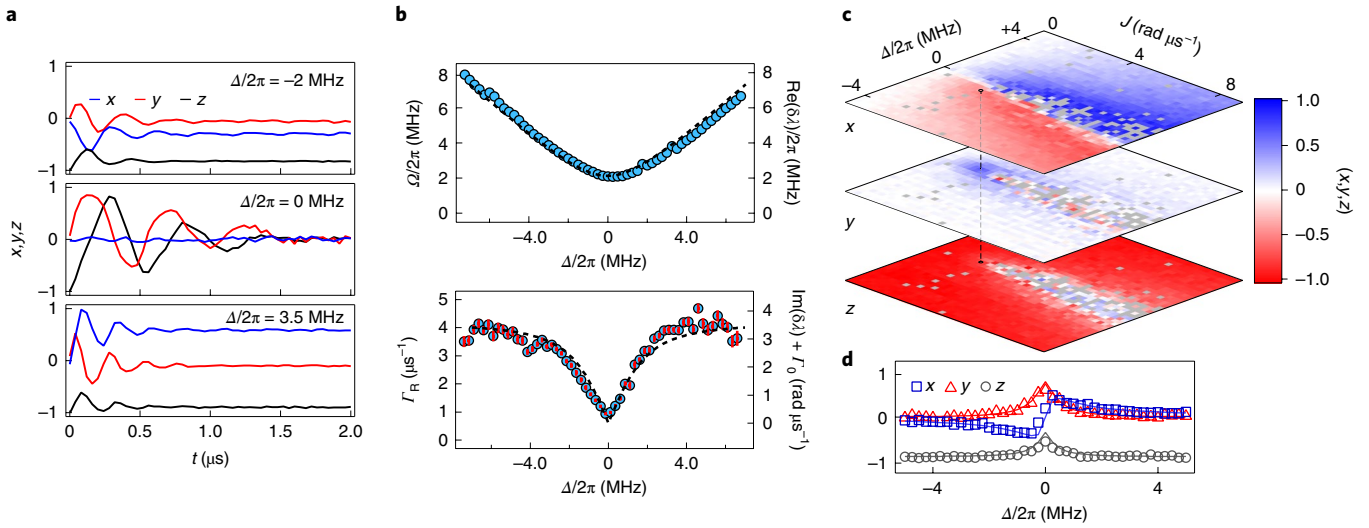

Fig. 4 | Coherence damping and steady state of a single dissipative qubit. a, Time evolution of the Bloch components are fit to decaying sinusoidal curves to extract Ω and Γ_R for different values of Δ. **b**, Observed Rabi frequencies and Γ_R versus Δ in the $\mathcal{PT}$-symmetric region for $J = 6.9\,\text{rad}\,\mu\text{s}^{-1}$ and $\gamma_e = 7.1\,\mu\text{s}^{-1}$. The dashed line in the top panel is the analytical result $\text{Re}(\delta\lambda)$; the dashed line in the bottom panel is the analytical result offset by the residual coherence-damping term, $\text{Im}(\delta\lambda) + \Gamma_0$. The error bars (vertical red lines, bottom panel) indicate the estimated error from the fit to a damped exponential function. **c**, Quantum state tomography of the qubit for an evolution time $t = 4\,\mu\text{s}$ shows the steady states reached for different parameter regimes. The dashed line indicates the location of the EP. Grey points indicate data points where there were insufficient numbers of successful post-selections. **d**, A line-cut across the EP as a function of Δ shows the steady-state Bloch coordinates x, y and z.

The observed Ω and Γ_R are in good agreement with the analytical predictions offset by Γ_0.

Quantum state tomography also allows us to study the steady states of the qubit system evolving under H_{eff} in the vicinity of the EP. Figure 4c displays the steady-state results of quantum state tomography after 4 μs of time evolution. Along the $\mathcal{PT}$-symmetric phase line ($\Delta = 0$ and $J > \gamma/4$), the qubit reaches a maximally mixed state. When $|\Delta| > 0$, the qubit reaches a mixed steady state in the X–Z plane, that is, $y \approx 0$. In close proximity of the EP, when γ_f approaches 0, the qubit reaches a steady state given by $(|e\rangle + i|f\rangle)/\sqrt{2}$, that is, the single eigenmode of H_{eff} at the EP (see Methods). In our experiment this appears as a peak in the y component in the tomography in Fig. 4c along with a vanishing x component and a z component that is suppressed in magnitude. These results indicate that the dissipation of the system stabilizes the qubit to non-trivial steady states for different drive and detuning parameters.

While the dynamics of the three-level transmon are described by a Lindblad equation with two dissipators that characterize spontaneous emission from levels $|f\rangle$ and $|e\rangle$, the non-Hermitian evolution and EP effects only manifest when quantum jumps to the $|e\rangle$ state are eliminated by post-selection[32]. This approach, combined with the toolbox of circuit quantum electrodynamics, serves as a versatile platform to explore fundamental questions in the quantum mechanics of open systems. Recent work identifying enhanced sensitivities in the vicinity of the EP has spurred interest in the role of quantum noise in EP-based sensors[33]. Our system forms an ideal platform for characterizing quantum sensing applications using non-Hermitian systems, including the role of noise introduced by dissipation (see Methods). Real-time control of parameters in H_{eff} will enable studies of the topological features associated with adiabatic perturbations that encircle the EP and of higher-order exceptional surfaces that arise in time-periodic (Floquet) non-Hermitian dynamics[11]. Finally, in concert with very recent work on superconducting circuits[34] and nitrogen–vacancy centres[35], our study provides the opportunity for non-Hermitian physics to play a leading role in a range of quantum information-processing applications.

Online content

Any methods, additional references, Nature Research reporting summaries, source data, statements of code and data availability and associated accession codes are available at https://doi.org/10.1038/s41567-019-0652-z.

Received: 26 January 2019; Accepted: 30 July 2019;
Published online: 7 October 2019

References

1. Rüter, C. E. et al. Observation of parity–time symmetry in optics. *Nat. Phys.* **6**, 192–195 (2010).
2. Regensburger, A. et al. Parity–time synthetic photonic lattices. *Nature* **488**, 167–171 (2012).
3. Hodaei, H., Miri, M.-A., Heinrich, M., Christodoulides, D. N. & Khajavikhan, M. Parity-time-symmetric microring lasers. *Science* **346**, 975–978 (2014).
4. Feng, L., Wong, Z. J., Ma, R.-M., Wang, Y. & Zhang, X. Single-mode laser by parity-time symmetry breaking. *Science* **346**, 972–975 (2014).
5. Peng, B. et al. Parity-time-symmetric whispering-gallery microcavities. *Nat. Phys.* **10**, 394–398 (2014).
6. Feng, L., El-Ganainy, R. & Ge, L. Non-Hermitian photonics based on parity-time symmetry. *Nat. Photon.* **11**, 752–762 (2017).
7. El-Ganainy, R. et al. Non-Hermitian physics and PT symmetry. *Nat. Phys.* **14**, 11–19 (2018).
8. Bender, C. M., Berntson, B. K., Parker, D. & Samuel, E. Observation of PT phase transition in a simple mechanical system. *Am. J. Phys.* **81**, 173–179 (2013).
9. Guo, A. et al. Observation of $\mathcal{PT}$-symmetry breaking in complex optical potentials. *Phys. Rev. Lett.* **103**, 093902 (2009).
10. Zeuner, J. M. et al. Observation of a topological transition in the bulk of a non-Hermitian system. *Phys. Rev. Lett.* **115**, 040402 (2015).
11. Li, J. et al. Observation of parity-time symmetry breaking transitions in a dissipative Floquet system of ultracold atoms. *Nat. Commun.* **10**, 855 (2019).
12. Weimann, S. et al. Topologically protected bound states in photonic parity-time-symmetric crystals. *Nat. Mater.* **16**, 433–438 (2016).
13. Xiao, L. et al. Observation of topological edge states in parity-time-symmetric quantum walks. *Nat. Phys.* **13**, 1117–1123 (2017).
14. Peng, B. et al. Loss-induced suppression and revival of lasing. *Science* **346**, 328–332 (2014).
15. Miao, P. et al. Orbital angular momentum microlaser. *Science* **353**, 464–467 (2016).

16. Wong, Z. J. et al. Lasing and anti-lasing in a single cavity. *Nat. Photon.* **10**, 796–801 (2016).
17. Wang, Z., Chong, Y., Joannopoulos, J. D. & Soljaić, M. Observation of unidirectional backscattering-immune topological electromagnetic states. *Nature* **461**, 772–775 (2009).
18. Rechtsman, M. C. et al. Photonic Floquet topological insulators. *Nature* **496**, 196–200 (2013).
19. Chang, L. et al. Parity–time symmetry and variable optical isolation in active–passive-coupled microresonators. *Nat. Photon.* **8**, 524–529 (2014).
20. Xu, H., Mason, D., Jiang, L. & Harris, J. Topological energy transfer in an optomechanical system with exceptional points. *Nature* **537**, 80–83 (2016).
21. Assawaworrarit, S., Yu, X. & Fan, S. Robust wireless power transfer using a nonlinear parity–time-symmetric circuit. *Nature* **546**, 387–390 (2017).
22. Hodaei, H. et al. Enhanced sensitivity at higher-order exceptional points. *Nature* **548**, 187–191 (2017).
23. Chen, W., Kaya Özdemir, S., Zhao, G., Wiersig, J. & Yang, L. Exceptional points enhance sensing in an optical microcavity. *Nature* **548**, 192–196 (2017).
24. Doppler, J. et al. Dynamically encircling an exceptional point for asymmetric mode switching. *Nature* **537**, 76–79 (2016).
25. Zhen, B. et al. Spawning rings of exceptional points out of Dirac cones. *Nature* **525**, 354–358 (2015).
26. Gao, T. et al. Observation of non-Hermitian degeneracies in a chaotic exciton-polariton billiard. *Nature* **526**, 554–558 (2015).
27. Kato, T. *Perturbation Theory for Linear Operators* (Springer, 1995).
28. Heiss, W. D. The physics of exceptional points. *J. Phys. A* **45**, 444016 (2012).
29. Zhang, D., Luo, X.-Q., Wang, Y.-P., Li, T.-F. & You, J. Q. Observation of the exceptional point in cavity magnon-polaritons. *Nat. Commun.* **8**, 1368 (2017).
30. Bender, C. M. & Boettcher, S. Real spectra in non-Hermitian Hamiltonians having *PT symmetry*. *Phys. Rev. Lett.* **80**, 5243–5246 (1998).
31. Mostafazadeh, A. Pseudo-Hermitian representation of quantum mechanics. *Int. J. Geom. Methods M* **7**, 1191–1306 (2010).
32. Dalibard, J., Castin, Y. & Mølmer, K. Wave-function approach to dissipative processes in quantum optics. *Phys. Rev. Lett.* **68**, 580–583 (1992).
33. Lau, H.-K. & Clerk, A. A. Fundamental limits and non-reciprocal approaches in non-Hermitian quantum sensing. *Nat. Commun.* **9**, 4320 (2018).
34. Partanen, M. et al. Optimized heat transfer at exceptional points in quantum circuits. Preprint at https://arxiv.org/abs/1812.02683 (2018).
35. Wu, Y. et al. Observation of parity-time symmetry breaking in a single-spin system. *Science* **364**, 878–880 (2019).

Acknowledgements

We thank P. M. Harrington for preliminary contributions, D. Tan for sample fabrication and K. Mølmer and C. Bender for discussions. K.W.M. acknowledges research support from the NSF (grant nos. PHY-1607156 and PHY-1752844 (CAREER)), and Y.N.J. acknowledges NSF grant no. DMR-1054020 (CAREER). This research used facilities at the Institute of Materials Science and Engineering at Washington University.

Author contributions

K.W.M., M.N. and Y.N.J. conceived the project. K.W.M., M.A. and M.N. performed the experiments and analysed the data. Y.N.J. provided theory support. K.W.M., M.N. and Y.N.J. wrote the manuscript.

Competing interests

The authors declare no competing interests.

Additional information

Supplementary information is available for this paper at https://doi.org/10.1038/s41567-019-0652-z.

Correspondence and requests for materials should be addressed to Y.N.J. or K.W.M.

Reprints and permissions information is available at www.nature.com/reprints.

Publisher's note: Springer Nature remains neutral with regard to jurisdictional claims in published maps and institutional affiliations.

Methods

Here, we provide details of the experimental set-up and techniques used in this work. We also provide an analysis of the system as described by a Lindblad evolution in the three-state manifold, which is equivalent to the non-Hermitian Hamiltonian evolution in the two-state manifold. We provide further discussion regarding the interplay of Lindbladian dissipation and non-Hermitian dissipation as well as prospects for enhanced sensing near the EP.

Experimental set-up. The transmon circuit[36,37] was fabricated by conventional double-angle evaporation and oxidation of aluminium on a silicon substrate. With zero flux threading the SQUID loop, the transition frequencies are $\omega_{g,e}/2\pi = 6.1$ GHz and $\omega_{e,f}/2\pi = 5.8$ GHz. The transmon circuit is placed in a three-dimensional copper cavity with frequency $\omega_{c,bare}/2\pi = 6.681$ GHz and decay rate $\kappa/2\pi = 5$ MHz with an embedded coil for adjusting the d.c. magnetic flux through the SQUID loop. The coupling rate between the transmon circuit and the cavity fields is $g/2\pi = 65$ MHz. Experiments are performed with a small flux threading the SQUID loop, resulting in $\omega_{g,e}/2\pi \approx 5.71$ GHz and $\omega_{e,f}/2\pi \approx 5.42$ GHz. These are given by the charging energy $E_c/h = 270$ MHz and the Josephson energy $E_J/h = 16.6$ GHz, where the dressed cavity resonance frequency is $\omega_c/2\pi = 6.684$ GHz. The dispersive coupling between the transmon and the cavity allows a high-fidelity, single-shot readout of the transmon states[38] and quantum state tomography[39]. The dispersive cavity resonance shifts are given by $\chi_e/2\pi = -2$ MHz and $\chi_f/2\pi = -11$ MHz. To rapidly resolve the transmon states with high fidelity, we use a Josephson parametric amplifier[40,41] operating in phase-sensitive mode with a 20 dB gain and an instantaneous bandwidth of 50 MHz. As shown in Supplementary Fig. 1, we are able to resolve the three transmon states with high fidelity.

Data analysis and experimental error. In Fig. 3 we extract the locations of the eigenstates in the broken and unbroken regions. This is achieved through a two-point measurement technique. In the unbroken region, the eigenstates are simply found by comparing the change in P_f^n over 500 ns of evolution. States that are stationary exhibit no change, whereas non-eigenstates exhibit oscillatory behaviour. In the broken regime, although the eigenvalues are strictly imaginary, the stationary states are still visible as regions where P_f^n is stationary. The data displayed in Fig. 3a have been scaled to account for the small γ_f decay over 500 ns. The preparation angles for the eigenstates were found from the zero crossing of the δP_f^n plots, determined from $\min(\mathrm{abs}(\delta P_f^n))$; the error bars indicate the distance to the next-nearest minima. For this dataset, $\gamma_e = 5.25\,\mu s^{-1}$ and $\gamma_f = 0.25\,\mu s^{-1}$.

Lindblad evolution of the three-state system. In the main text, we focused solely on the dynamics in a qubit subsystem that is governed by H_{eff} (equation (1)). Instead, one can look at the dynamics for the entire three-level system, which can be described by a Lindblad master equation ($\hbar = 1$) (refs. [42,43]):

$$\dot{\rho} = -i[H_c, \rho] + \sum_{k=e,f}\left[L_k \rho L_k^\dagger - \frac{1}{2}\{L_k^\dagger L_k, \rho\}\right] \tag{2}$$

where $\rho(t)$ is a 3×3 density matrix, $\dot{\rho}$ is the time derivative, and $H_c = J(|e\rangle\langle f| + |f\rangle\langle e|) - \Delta/2(|f\rangle\langle f| - |e\rangle\langle e|)$ is a coupling Hamiltonian with Δ in the rotating frame. The Lindblad dissipation operators $L_e = \sqrt{\gamma_e}|g\rangle\langle e|$ and $L_f = \sqrt{\gamma_f}|e\rangle\langle f|$ account for the energy decay from level $|e\rangle$ to $|g\rangle$ and from $|f\rangle$ to $|e\rangle$, respectively, and the dagger represents the Hermitian conjugate. Equation (2) leads to the following closed set of equations for the dynamics of the qubit levels:

$$\begin{aligned}
\dot{\rho}_{ff} &= -iJ(\rho_{ef} - \rho_{fe}) - \gamma_f \rho_{ff} \\
\dot{\rho}_{ee} &= +iJ(\rho_{ef} - \rho_{fe}) - \gamma_e \rho_{ee} + \gamma_f \rho_{ff} \\
\dot{\rho}_{ef} &= -iJ(\rho_{ff} - \rho_{ee}) - (\gamma_e + \gamma_f + 2i\Delta)/2\rho_{ef} \\
\dot{\rho}_{fe} &= +iJ(\rho_{ff} - \rho_{ee}) - (\gamma_e + \gamma_f - 2i\Delta)/2\rho_{fe}
\end{aligned} \tag{3}$$

Since the drive only acts on the manifold of two excited states, the dynamics of the ground state are decoupled from the upper manifold. For a given initial condition, one can solve equation (3) to obtain the evolution of any observable. As in the experiment where the system is initialized in the state $|f\rangle$ and in the limit of $\gamma_f \ll \gamma_e$ and where $\Delta = 0$, the evolutions for the populations of each level in the $\mathcal{PT}$-symmetric phase are given by

$$P_e = \rho_{ee} = e^{-\frac{\gamma_e}{2}t}\left(\frac{J}{\alpha}\right)^2 \sin^2(\alpha t) \tag{4}$$

$$P_f = \rho_{ff} = e^{-\frac{\gamma_e}{2}t}\left(\frac{J}{\alpha}\right)^2 \cos^2(\alpha t - \theta) \tag{5}$$

where $\alpha = \sqrt{J^2 - (\gamma_e/4)^2}$ and $\theta = \arcsin(\gamma_e/4J)$.

In the main text, all analysis is performed in a model-independent manner; the evolution of the post-selected occupation number $P_f^n(t)$ is fit to an exponentially decaying sine function to determine the coherence-decay rate and the Rabi oscillation frequency. With access to the exact evolution in the three-state system, we can determine the actual form for the oscillation in the sub-manifold (for example Fig. 2c). From equations (4) and (5) we can obtain the normalized population

$$P_f^n = \frac{P_f}{P_f + P_e} = \frac{\cos^2(\alpha t - \theta)}{\sin^2(\alpha t) + \cos^2(\alpha t - \theta)} \tag{6}$$

In the limit of $J \gg \gamma_e \gg \gamma_f$, equation (6) reduces to $\cos^2(Jt)$, which means that deep in the $\mathcal{PT}$-symmetric region far from the EP, the population oscillates with a frequency of $2J$. The observed oscillation frequency at $J \gg \gamma_e$ was used to calibrate the values of J for weaker drives. These results are consistent with the direct theoretical approach for the evolution of the qubit wave function under H_{eff}.

Quantum state tomography in the vicinity of the EP. Figure 4c displays quantum state tomography for a fixed evolution time $t = 4\,\mu s$ as a function of Δ and J. At $t = 4\,\mu s$, the number of successful post-selections can be quite low, especially at $\Delta = 0$, where the evolution takes the qubit through the lossy $|e\rangle$ state.

Supplementary Fig. 2 displays comparisons of the tomography data with simulations that use equation (3) for the same evolution time $t = 4\,\mu s$. Oscillations for $\Delta = 0$ have not completely damped out for this evolution time. We attribute the faster damping in the experimental data to additional dephasing, characterized by Γ_0, which was not included in the simulation. We otherwise see good qualitative agreement between the simulation and the experimental data.

We also measured Γ_0 for a different flux bias of the transmon where $\gamma_e = \gamma_f = 0.14\,\mu s^{-1}$ and found $\Gamma_0 = 0.46\,\mu s^{-1}$ for $J = 6.9\,\mathrm{rad}\,\mu s^{-1}$, which is in fairly close agreement with what was observed in Fig. 4. From this we conclude that the additional dephasing is probably due to flux or charge noise in the transmon and not a feature of the effective non-Hermitian evolution.

Interplay between L_e and L_f. The combination of non-Hermitian evolution and dissipation is shown to produce a steady state of the qubit along the $+\hat{y}$ axis by quantum state tomography (Fig. 4c). We examine this feature through simulations of the Lindblad master equation for the three-state system where both L_e and L_f are present with comparable magnitudes. In Supplementary Fig. 3a we display the steady state of the Bloch coordinate y as a function of Δ for $J = (\gamma_e - \gamma_f)/4$, which corresponds to the EP for $\Delta = 0$. We observe that while γ_f is necessary for the formation of a steady state, the steady-state coherence is maximal for extremal ratios of γ_e/γ_f. Supplementary Fig. 3b displays a similar calculation, but for different values of γ_f. We observe that at $\gamma_f = \gamma_e/2$, the steady-state Bloch coordinate y changes sign, approaching that expected for a normal dissipative qubit where the balance of drive and decay can result in a steady-state coherence[44] with a negative y. This transition occurs when the Lindbladian dissipation overtakes the non-Hermitian dissipation, which occurs at $\gamma_f = \gamma_e/2$.

Quantum sensing in the vicinity of the EP. Recent work with classical systems has indicated that EP degeneracies may yield measurement advantages[22,45,46]. These studies have motivated further investigation into whether these advantages persist in the fully quantum regime where quantum noise dominates the measurement process. Theoretical work on semiclassical optical systems[33,47] has found that enhanced sensitivities near the EP are counteracted by enhanced fluctuations, curtailing measurement advantages. How these studies extend to the fully quantum regime explored here remains an open question. In this section, we briefly discuss how the Lindblad evolution of the three-state system can be used to characterize enhanced measurement sensitivities in terms of the quantum Fisher information (QFI) and how the post-selection process may hamper these advantages.

In quantum metrology, the Cramér–Rao bound[48] gives a universal limit for the mean squared deviation in the estimate of a parameter:

$$\langle \delta^2 \hat{g} \rangle \geq \frac{1}{\nu I_g^{(Q)}} \tag{7}$$

where ν is a measure of the amount of data, $\hat{g}$ is an unbiased estimator of the parameter g formed from measurement data and $I_g^{(Q)}$ is the QFI, which can be expressed in terms of the Bures distance, ds^2 (ref. [49]), $ds^2 = 2(1 - |\langle \psi_g | \psi_{g+dg} \rangle|)$, where $|\psi_g\rangle$ the state after evolution under parameter g, and $|\psi_{g+dg}\rangle$ the state after evolution under parameter $g+dg$, $I_g^{(Q)} = 4ds^2/dg^2$.

One approach to metrology near the EP is based on Rabi interferometry. For this, we consider preparing the qubit in state $|f\rangle$ and allowing evolution under H_{eff} for certain durations of time. Supplementary Fig. 4a displays the evolution of P_f^n for parameter regimes that are near the EP calculated using equation (3) for the three-state system. The evolution near the EP is not purely sinusoidal; there are points where the f-state population varies rapidly with time. When J is changed by a small amount, we observe a large change in the f-state population compared with the case of a normal Hermitian qubit with no EP for the same evolution time. The fractional change in the f-state population with a fractional change in J is closely related to the QFI.

To determine the QFI, we simply vary J by a small amount to determine the slope dP_f^n/dJ. For small changes near $P_f^n = 0.5$, we have

$P_f^{n_{-\frac{1}{2}}} = \cos(d\theta/2)\sin(d\theta/2) \approx d\theta/2$, where $d\theta$ is a small change in the polar angle near the equator of the Bloch sphere. Thus, near the equator of the Bloch sphere, the QFI about the coupling rate J is simply given by $I_J^{(Q)} = (dP_f^n/dJ)^2$.

Supplementary Fig. 4b displays the QFI for this measurement scheme near the EP using the parameters in Supplementary Fig. 4a. The QFI diverges near the EP, as has been observed for the classical Fisher information in classical systems. This improved QFI comes at a cost, however, due to the post-selection that is used to realize the effective non-Hermitian dynamics; near the EP, the post-selection efficiency is low, which ultimately decreases the amount of data available. The enhanced sensitivity near the EP bears similarities to weak value amplification, where low post-selection efficiency is at odds with amplified signals. Even in this case, there are advantages to post-selection when signals are dominated by technical noise[50].

Data availability

The data that support the plots within this paper and other findings of this study are available from K.W.M. on reasonable request.

References

36. Koch, J. et al. Charge-insensitive qubit design derived from the Cooper pair box. *Phys. Rev. A* **76**, 042319 (2007).
37. Paik, H. et al. Observation of high coherence in Josephson junction qubits measured in a three-dimensional circuit QED architecture. *Phys. Rev. Lett.* **107**, 240501 (2011).
38. Wallraff, A. et al. Approaching unit visibility for control of a superconducting qubit with dispersive readout. *Phys. Rev. Lett.* **95**, 060501 (2005).
39. Steffen, M. et al. Measurement of the entanglement of two superconducting qubits via state tomography. *Science* **313**, 1423–1425 (2006).
40. Castellanos-Beltran, M. A., Irwin, K. D., Hilton, G. C., Vale, L. R. & Lehnert, K. W. Amplification and squeezing of quantum noise with a tunable Josephson metamaterial. *Nat. Phys.* **4**, 929–931 (2008).
41. Hatridge, M., Vijay, R., Slichter, D. H., Clarke, J. & Siddiqi, I. Dispersive magnetometry with a quantum limited SQUID parametric amplifier. *Phys. Rev. B* **83**, 134501 (2011).
42. Jacobs, K. *Quantum Measurement Theory and its Applications* (Cambridge University Press, 2014).
43. Wiseman, H. & Milburn, G. *Quantum Measurement and Control* (Cambridge University Press, 2010).
44. Carmichael, H. J., Lane, A. S. & Walls, D. F. Resonance fluorescence from an atom in a squeezed vacuum. *Phys. Rev. Lett.* **58**, 2539–2542 (1987).
45. Wiersig, J. Enhancing the sensitivity of frequency and energy splitting detection by using exceptional points: application to microcavity sensors for single-particle detection. *Phys. Rev. Lett.* **112**, 203901 (2014).
46. Chen, C., Jin, L. & Liu, R.-B. Sensitivity of parameter estimation near the exceptional point of a non-Hermitian system. *New J. Phys.* **21**, 083002 (2019).
47. Zhang, M. et al. Quantum noise theory of exceptional point sensors. Preprint at https://arxiv.org/abs/1805.12001 (2018).
48. Cramér, H. *Mathematical Methods of Statistics* (Princeton University Press, 1946).
49. Bures, D. An extension of Kakutani's theorem on infinite product measures to the tensor product of semifinite w*-algebras. *T. Am. Math. Soc.* **135**, 199–212 (1969).
50. Jordan, A. N., Martnez-Rincón, J. & Howell, J. C. Technical advantages for weak-value amplification: when less is more. *Phys. Rev. X* **4**, 011031 (2014).